International Journal of Thermophysics (2026) 47:76
https://doi.org/10.1007/s10765-026-03754-2

Intrinsic Thermal Anisotropy Ratio of Graphene-Based µm-Thick Films

Mahya Rahbar[1] · Amin Karamati[1] · Jiwen Li[2] · Lijun Zhang[3] · Xinwei Wang[1]

Received: 26 March 2026 / Accepted: 30 March 2026

Abstract

The thermal conductivity (k) of graphene-based layered µm-thin structures, termed "paper", is highly anisotropic, and strongly varies from sample to sample. In addition to k, the thermal anisotropy ratio ($\Theta = k_{max}/k_{min}$) is also a critical property reflecting the material's structure and is of great importance in thermal design. The intrinsic Θ determination requires in-situ measurement of both in-plane k ($k_{\parallel}$) and out-of-plane k ($k_{\perp}$) of the same sample. Such intrinsic Θ knowledge is not much available to date. In this work, graphene paper (GP), graphene oxide paper (GOP), and partly reduced graphene paper (PRGP) are investigated, each exhibiting distinct microstructural features arising from different oxidation and reduction states. These structural variations lead to pronounced differences in both the magnitude and anisotropy of k, highlighting the strong influence of oxidation-induced disorder on directional thermal transport. A photothermal approach is employed to measure both $k_{\parallel}$ and $k_{\perp}$ of the same suspended micro-thick samples by tuning the modulation frequency to selectively enhance sensitivity to in-plane or out-of-plane heat conduction. Because both $k_{\parallel}$ and $k_{\perp}$ are obtained from a single specimen and a fixed laser position, structural variation associated with multi-sample preparation is eliminated, enabling reliable determination of the intrinsic Θ. The measured $k_{\perp}$ and $k_{\parallel}$ are 7.28 and 690 $W{\cdot}m^{-1}{\cdot}K^{-1}$ for GP ($\Theta = 94.8$), 0.215 and 0.78 $W{\cdot}m^{-1}{\cdot}K^{-1}$ for GOP ($\Theta = 3.63$), and 0.316 and 2.9 $W{\cdot}m^{-1}{\cdot}K^{-1}$ for PRGP ($\Theta = 9.18$), respectively. The significantly reduced k and Θ of GOP is attributed to enhanced phonon scattering from oxygen-containing functional groups, while GP exhibits the highest k and Θ due to its high crystallinity.

Keywords Anisotropic thermal conductivity · Frequency-resolved measurement · Graphene-based structure · Thermal anisotropy ratio

Mahya Rahbar and Amin Karamati have contributed equally to this work.

Extended author information available on the last page of the article

Published online: 13 April 2026

1 Introduction

Many materials exhibit anisotropic structures, meaning their properties vary with directions due to differences in crystal structure, microstructure, or composition [1]. Accurate knowledge of anisotropic thermal conductivity is essential for heat flow analysis, thermal modeling, and device design [2, 3] particularly in applications such as transistors [4], electronic devices [5], and high temperature superconductors [6], where efficient heat dissipation is essential for enhancing performance and reliability [7]. Graphene-based papers are a representative class of anisotropic materials, in which layered morphology gives rise to strong directional thermal transport. However, their effective thermal conductivity is highly sensitive to oxidation level, defect density, and interlayer coupling. Variations in chemical functionalization and reduction history can significantly alter phonon scattering, leading to wide discrepancies in reported thermal conductivity values even among nominally similar graphene-based materials.

A wide range of experimental techniques have been developed to characterize anisotropic thermal conductivity of materials. For example, Chowdhury et al. [8] measured the anisotropic thermal conductivity of micrometer-thick polyimide (PI) films by combining frequency-domain probe beam deflection (FD-PBD) for in-plane measurements with time-domain thermoreflectance (TDTR) for cross-plane measurements [9, 10]. Tian and Cole [11] employed the 3ω technique [12] to investigate anisotropic thermal transport in millimeter-thick carbon fiber/epoxy composites, utilizing different excitation frequencies to enhance sensitivity to either in-plane or cross-plane heat conduction. Similarly, Jang et al. [13] used two variations of TDTR to measure the anisotropic thermal conductivity of exfoliated black phosphorus, relying on different laser spot sizes, modulation frequencies, and beam-offset configurations to resolve directional thermal transport. Related TDTR/FDTR-based strategies using variable spot sizes or beam offsets have also been applied to a variety of anisotropic materials [14, 15]. Other approaches combine fundamentally different techniques to access thermal transport along different directions. Huang et al. [16] measured the anisotropic thermal conductivity of suspended two-dimensional tellurium films using micro-Raman thermometry for in-plane transport and TDTR for cross-plane transport, requiring separate sample configurations and transducer deposition. It has also been reported that pump–probe techniques are often time-consuming due to repetitive data acquisition [9, 17], and typically operate at high modulation frequencies, making them more sensitive to cross-plane measurements [14]. In addition, probe-beam reflectivity requirements often necessitate smooth sample surfaces. To address some of these limitations, Wang et al. [18] introduced spatially resolved lock-in microthermography (SR-LIT) for rapid in-plane thermal characterization, while Takahashi et al. [19] and Tanimoto et al. [20] employed temperature-wave-based techniques to measure in-plane and cross-plane thermal diffusivities using different experimental arrangements. Despite these advances, many existing approaches rely on multiple techniques, distinct frequency regimes, or separate sample preparations to resolve in-plane and cross-plane thermal conductivities. Such

requirements increase experimental complexity and can introduce uncertainties when material microstructure varies between samples or preparation steps. These limitations are particularly critical for graphene-based papers, where oxidation level, defect density, and flake alignment can vary subtly yet significantly influence directional phonon transport. Also such structure's rough surface makes it hard to employ the TDTR/FDTR-based and 3ω techniques for simultaneously measuring both the in-plane and out-of-plane thermal conductivities.

Accurately characterizing thermal anisotropy of graphene-based papers remains challenging, largely due to sample preparation constraints. Many prior studies rely on separate samples or distinct preparation routes to measure in-plane and cross-plane thermal conductivities. Even when samples originate from the same parent material, variations introduced during cutting, handling, or post-processing can alter microstructure, making it difficult to reliably capture the intrinsic anisotropic properties of a single specimen. In our previous studies on polypropylene separators for lithium-ion batteries [21] and gas diffusion layers in proton exchange membrane fuel cells [22], in-plane and cross-plane thermal conductivities are measured using the transient electro-thermal (TET) [23] and differential thermal resistance (DTR) techniques [24], respectively. While effective, this multi-technique approach is time-consuming, costly, and requires separate sample preparations, which can obscure true material anisotropy when sample-to-sample structure variations are non-negligible. To overcome these limitations, in this work, we employ a unified experimental framework capable of extracting both in-plane and cross-plane thermal conductivities from the same specimen using a single prepared sample and a fixed measurement location. This approach eliminates preparation-induced structure variation and enables a more faithful assessment of intrinsic thermal anisotropy ratio (Θ). Using this framework, anisotropy factors are systematically reported for graphene paper (GP), graphene oxide paper (GOP), and partly reduced graphene paper (PRGP), and directly correlated with their structural and chemical differences. Raman spectroscopy and optical microscopy reveal distinct degrees of oxidation, disorder, and flake alignment among these materials, which are expected to strongly influence both in-plane and cross-plane phonon transport. The measurements are based on a photothermal (PT) technique [25, 26], in which the modulation frequency is tuned to selectively enhance sensitivity to either in-plane or cross-plane heat flow, allowing both components to be resolved within a single experimental configuration.

2 Materials and Methods

2.1 Sample Structure

In this work, we conduct measurements of graphene paper (GP), graphene oxide paper (GOP), and partly reduced graphene paper (PRGP). The GP sample is purchased from Graphene Supermarket, while the GOP and PRGP samples are obtained from ACS Materials. The GP sample has a thickness of 31 μm, measured using a digital micrometer with 1 μm accuracy. It consists of stacked layers of pure graphene sheets with a shiny surface. The GOP sample, with a thickness

of 20 µm, contains oxygen-based functional groups and is produced by a modified Hummer's method [27] using direct flow. The PRGP sample, with a thickness of 10 µm, is partially reduced graphene oxide, where some of the oxygen-containing groups have been removed to partially restore the graphene structure. Figure 1a shows the Raman spectra of all three samples at 532 nm excitation, highlighting distinct differences. For GP, as shown in Fig. 1b, the two strongest peaks are the G band at 1580 cm^{-1} and the 2D band around 2719 cm^{-1}. The absence of the D band, which comes from the breathing mode of aromatic rings [28], indicates that the sample is highly crystalline and shows minimal structural disorder. The G peak is common in all carbon-based materials and represents carbon–carbon bond vibrations. The 2D peak is the second-order overtone of the D band, not related to defects, and results from a two-phonon lattice vibration process. In single-layered graphene, the 2D peak is sharp and single. As the number of layer increases, the peak becomes broader. The ratio of the integrated intensities of the G and 2D bands (I_G/I_{2D}) helps estimate the number of graphene layers. For the GP sample, this ratio is calculated to be 0.76, which corresponds to ~6–7 layers within the graphene flakes. Note that HOPG has an I_G/I_{2D} ratio of 0.86 [29].

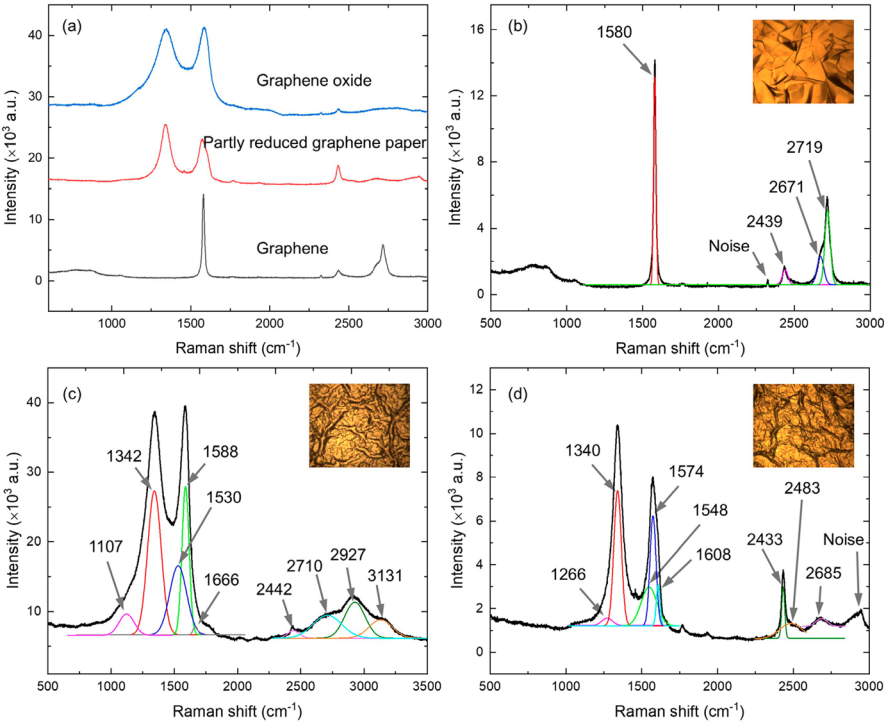

Fig. 1 (a) Raman spectra of GP, GOP, and PRGP together under 532 nm excitation, showing distinct spectral features. Fitted peaks for (b) GP, (b) GOP, and (d) PRGP. The insets are optical images of each sample taken under a 20×objective lens

The Raman spectra of the GOP sample, shown in Fig. 1c, indicates low crystallinity, as evidenced by the broad D band at 1342 cm^{-1}. The width of the D peak increases with a higher degree of oxidation, which corresponds to more defects in the graphene oxide structure [30]. The D* band at 1107 cm^{-1} arises due to defect-activated phonons in the longitudinal acoustic (LA) branch near the *K* point, involved in an intervalley double resonance process. The D' band at 1666 cm^{-1} is related to an intravalley one-phonon double resonance process [31]. The D″ band at 1530 cm^{-1} is associated with amorphous carbon phases, and its intensity and width decreases as crystallinity increases [32, 33]. Our observed peaks align well with those reported by Claramunt et al. [34]. According to literature, in graphene of high-level disorder, the intensity of the 2D band decreases and is often replaced by a broad bump [35]. In the GOP sample, we observe the 2D band at 2710 cm^{-1}, a combination band (D + D′) band at 2927 cm^{-1}, and the overtone band 2D′ at 3131 cm^{-1}, which agree with findings by Lopes-Diaz et al. [36]. The D + D′ results from the combination of phonons with different momentum and is only active in the presence of defects. In contrast, the 2D and 2D′ bands do not require defects for activation. Additionally, a weak G* band appears at 2442 cm^{-1}, consistent with previous reports. This band arises from a double resonance intervalley process involving an in-plane transverse optical (iTO) phonon and a LA phonon [37].

Figure 1d shows the Raman spectra of the PRGP sample, which closely matches the results reported in Ref. [38]. The differences between the Raman spectra of GOP and PRGP reflect significant structural changes due to the reduction process. Specifically, the G and D bands in PRGP are narrower than those in GOP, indicating a decrease in defects, which is mainly the removal of oxygen-containing groups. Our Spectrum is similar to that of a low reduction of graphene oxide (GO) sample, as reported by Scardaci and Compagnini [28, 39]. The insets of Fig. 1b–d show optical images of each sample taken under a 20× objective lens, where surface differences are also evident. The GP sample has flakes of high crystalline structure while the GOP and PRGP samples have very disordered surface structure. These structural differences between the samples also cause different thermophysical properties, which will be discussed in the following sections.

The structural differences observed from Raman spectroscopy can be further supported by X-ray diffraction (XRD), which provides insight into interlayer ordering and spacing. XRD results reported by Xie et al. [40] for the same materials show that for GP, a sharp (002) diffraction peak at ~ 26.6° corresponds to an interlayer spacing of ~ 3.35 Å, similar to graphite, indicating a highly ordered graphitic structure with strong interlayer coupling. In contrast, oxidation in GOP introduces oxygen-containing functional groups that expand the interlayer spacing through the insertion of these groups between graphene layers. This expansion weakens the van der Waals interactions and disrupts the stacking order, thereby suppressing phonon transport both in-plane and across layers. For GOP, the major diffraction peak shifts to ~ 10.52°, corresponding to a significantly increased interlayer spacing of ~ 8.40 Å. In PRGP, partial removal of oxygen functional groups leads to a partial restoration of the layered structure. However, residual defects and enlarged interlayer spacing continue to limit phonon transport compared to GP.

2.2 Physical Model for Thermal Conductivity Measurements

The PT technique is employed here to simultaneously measure the both cross-plane and in-plane thermal conductivities by varying the modulation frequency of the laser irradiation on the sample. As shown in Fig. 2a, the film-like sample is suspended over two stands and secured using silver paste to ensure excellent mechanical and thermal contacts. A modulated laser beam is irradiating the middle part of the sample, and the local surface thermal radiation is collected and measured. The phase shift of the thermal radiation relative to the laser beam is strongly affected by the heat conduction in the sample, and can be used to determine the desired thermal conductivity. At higher frequencies, the in-plane thermal diffusion length becomes smaller than the laser spot size, making the heat flow predominantly along the cross-plane direction. As illustrated in Fig. 2a, under these conditions, the lateral heat transfer is limited, and the detected thermal radiation signal mainly reflects the cross-plane thermal transport. Conversely, at lower frequencies, the in-plane thermal diffusion length significantly exceeds the laser spot size, enhancing sensitivity to in-plane heat transfer, as shown in Fig. 2b. In this case, heat primarily spreads laterally along the sample surface and the temperature gradient is negligible in the cross-plane direction. Additional details regarding the frequency selection and sensitivity analysis are provided in Sect. 3.2.

2.2.1 Cross-Plane Direction Thermal Conductivity Measurement

Figure 2c shows the schematic of a multilayer sample structure used for 1D heat transfer modeling in the PT technique for the cross-plane thermal conductivity measurements. In a typical PT experiment, the structure consists of $N+2$ layers, where layer 0 is the backing material (e.g., air or a substrate), and layer $N+1$ represents the surrounding air or vacuum. In this study, the measurements are conducted under vacuum conditions, so both layer 0 and layer $N+1$ correspond to vacuum or a low-pressure environment with minimal air presence. The thickness of each layer is denoted as $Z_i = z_i - z_{i-1}$.

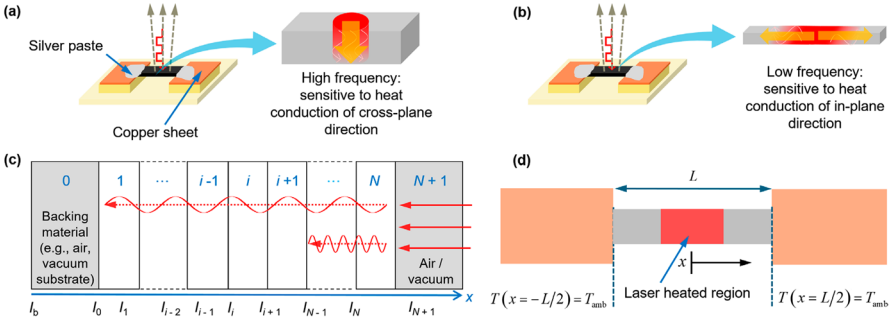

Fig. 2 (a) Physical principle illustrating that cross-plane thermal conductivity is governed at higher frequencies, and (b) in-plane thermal conductivity is governed at lower frequencies. (c) Schematic of the N-layer sample used in the cross-plane heat transfer model, and (d) schematic of the sample configuration used in the in-plane heat transfer model

Key thermal and optical properties considered for each layer include cross-plane thermal conductivity ($k_{\perp,i}$), specific heat ($c_{p,i}$), thermal diffusivity (α_i), optical absorption coefficient (β_i), thermal diffusion length ($\mu_i = \sqrt{\alpha_i / (\pi f)}$), thermal diffusion coefficient ($a_i = 1/\mu_i$), and thermal contact resistance between layer i and $i+1$ ($R_{i,i+1}$). The modulation frequency of the incident laser is denoted as f, with the angular frequency of $\omega = 2\pi f$. The governing equation for 1D thermal diffusion in layer i is [25]

$$\frac{\partial^2 \theta_i}{\partial x^2} = \frac{1}{\alpha_i}\frac{\partial \theta_i}{\partial t} - \frac{\beta_i I_0}{2k_{\perp,i}} \exp\left(-\sum_{m=i+1}^{N} \beta_m Z_m\right) \cdot \exp\left[\beta_i (x - z_i)\right] \cdot \left[1 + e^{j\omega t}\right]. \quad (1)$$

Here, $\theta_i = T_i - T_{\text{amb}}$ represents the temperature rise of layer i, T_{amb} is the ambient temperature. The solution to this equation consists of three parts: the transient component ($\theta_{i,t}$), which decays as the system approaches thermal steady state, a steady DC component ($\overline{\theta}_{i,s}$), and a steady AC component ($\tilde{\theta}_{i,s}$), which oscillates with the laser modulation frequency and is used for measuring thermal properties. Only the AC component is measured using a lock-in amplifier and used for further analysis. The general solution for $\tilde{\theta}_{i,s}$ is

$$\tilde{\theta}_{i,s} = \left[A_i e^{\sigma_i (x - z_i)} + B_i e^{-\sigma_i (x - z_i)} - E_i e^{\beta_i (x - z_i)}\right] e^{j\omega t}, \quad (2)$$

$$E_i = G_i / \left(\beta_i^2 - \sigma_i^2\right), \quad (3)$$

$$G_i = \beta_i I_0 \exp\left(-\sum_{m=i+1}^{N} \beta_m Z_m\right) \Big/ \left(2k_{\perp,i}\right), \quad (4)$$

where σ_i is defined as $(1+j)a_i$, and $j = \sqrt{-1}$, and we have $G_N = \beta_N I_0 / 2k_{\perp,N}$ ($i < N$) and $G_{N+1} = 0$.

The coefficients A_i and B_i carry information about the sample's thermal and optical characteristics. These are calculated using an interfacial transmission matrix of heating (U_i) and absorption matrix of light from layer $i+1$ to i (V_i). Assuming that both vacuum environments (layer 0 and $N+1$) are thermally thick, which is valid in our experimental setup, then we have $A_{N+1} = 0$ and $B_0 = 0$. This allows the remaining coefficients (A_i and B_i) to be determined at $x = z_i$ as

$$\begin{bmatrix} A_i \\ B_i \end{bmatrix} = U_i \begin{bmatrix} A_{i+1} \\ B_{i+1} \end{bmatrix} + V_i \begin{bmatrix} E_i \\ E_{i+1} \end{bmatrix}, \quad (5)$$

$$U_i = \frac{1}{2}\begin{bmatrix} u_{11,i} & u_{12,i} \\ u_{21,i} & u_{22,i} \end{bmatrix}, \quad (6)$$

$$V_i = \frac{1}{2}\begin{bmatrix} v_{11,i} & v_{12,i} \\ v_{21,i} & v_{22,i} \end{bmatrix}. \tag{7}$$

$$u_{1n,i} = \left(1 \pm k_{\perp,i+1}\sigma_{i+1} \big/ k_i\sigma_i \mp k_{\perp,i+1}\sigma_{i+1}R_{i,i+1}\right) \cdot \exp\left[\mp\sigma_{i+1}\left(z_{i+1} - z_i\right)\right], \quad n = 1, 2, \tag{8}$$

$$u_{2n,i} = \left(1 \mp k_{\perp,i+1}\sigma_{i+1} \big/ k_{\perp,i}\sigma_i \mp k_{\perp,i+1}\sigma_{i+1}R_{i,i+1}\right) \cdot \exp\left[\mp\sigma_{i+1}\left(z_{i+1} - z_i\right)\right], \quad n = 1, 2, \tag{9}$$

$$v_{1n,i} = \left(-1 \mp \beta_i \big/ \sigma_i\right), \quad n = 1, 2, \tag{10}$$

$$v_{2n,i} = \left(-1 \mp k_{\perp,i+1}\beta_{i+1} \big/ k_{\perp,i}\sigma_i \mp k_{\perp,i+1}\beta_{i+1}R_{i,i+1}\right) \cdot \exp\left[-\beta_{i+1}\left(z_{i+1} - z_i\right)\right], \quad n = 1, 2. \tag{11}$$

Finally, the coefficients A_i and B_i can be expressed as

$$B_{N+1} = -\frac{\begin{bmatrix} 0 & 1 \end{bmatrix} \sum_{m=0}^{N} \left(\prod_{i=0}^{m-1} U_i \right) V_m \begin{bmatrix} E_m \\ E_{m+1} \end{bmatrix}}{\begin{bmatrix} 0 & 1 \end{bmatrix} \prod_{i=0}^{m-1} U_i \begin{bmatrix} 0 \\ 1 \end{bmatrix}}, \tag{12}$$

$$\begin{bmatrix} A_i \\ B_i \end{bmatrix} = \left(\prod_{m=i}^{N} U_m \right) \begin{bmatrix} 0 \\ B_{N+1} \end{bmatrix} + \sum_{m=i}^{N} \left(\prod_{k=i}^{m-1} U_k \right) V_m \begin{bmatrix} E_m \\ E_{m+1} \end{bmatrix}. \tag{13}$$

The PT signal is directly linked to the surface temperature of the sample, as the emitted thermal radiation is proportional to surface temperature fluctuations, especially when the temperature rise is small. By applying Eq. 2 from the 1D heat transfer model and using trial values for unknown parameters such as thermal conductivity and optical absorption length, the theoretical phase shift can be calculated for each modulation frequency. These theoretical phase shift values are then compared with the experimentally measured ones. The difference between them is quantified by calculating the sum of squared errors. The best-fit material properties are determined by minimizing this sum, resulting in the parameter set that most closely matches the experimental data. Note that in the simulation, the laser irradiates layer *N*, and the phase shift measured for temperature response analysis also corresponds to layer *N*.

2.2.2 In-Plane Direction Thermal Conductivity Measurement

The schematic of the sample configuration used in the in-plane heat transfer model is shown in Fig. 2d. For the in-plane thermal conductivity measurements, the heat conduction is modeled as 1D heat transient in the length direction and is governed by Refs. [41, 42]

$$k_{\parallel}\frac{\partial^2 T}{\partial x^2}+\dot{q}=\rho c_p\frac{\partial T}{\partial t}, \tag{14}$$

where ρ is the density, c_p is the specific heat capacity, $k_{\parallel}$ is the in-plane thermal conductivity, and $\dot{q}$ is the volumetric heat generation due to the laser absorption. Although the laser is absorbed in a surface region of tens of nm thickness, the modulation frequency is low, so the heat transfer quickly reaches equilibrium in the thickness direction. Therefore, this volumetric heat generation approximation across the thickness direction will not affect the final solution, while it can significantly simplify the problem solving. This 1D heat conduction is reasonable since our sample's width is small, and the laser beam fully covers the width in the irradiation region. The laser is modulated periodically, and the spatial and temporal form of the source is given by

$$\dot{q}(x,t)=\dot{q}_0\exp\left[-\left(x-x_0\right)^2\Big/ r_0^2\right]\cdot\Psi. \tag{15}$$

here, $\dot{q}_0$ is the peak heating rate at the center of the laser beam, r_0 is the laser spot radius corresponding to the e^{-1} peak intensity and x_0 is the beam center, which will be discussed later. Ψ is the laser modulation function. In the experiment, the laser is modulated as a square wave at varying frequencies. However, for frequency-domain analysis, the temperature response at the fundamental frequency is of primary interest. Therefore, for mathematical treatment purpose, Ψ is expressed as $e^{i\omega t}$, and the resulting steady-periodic response is extracted. The governing equation is solved in the frequency domain to obtain the complex temperature amplitude, which provides both the magnitude and the phase of the temperature oscillation in response to the modulated laser heating. Since the infrared detector collects radiation over a finite region (1 mm), the detected signal is modeled as the spatial average of the complex temperature over this sensing length. The phase shift of the temperature response relative to modulated laser beam is then compared with the experimental data to extract the in-plane thermal conductivity via least-square fitting. The frequency-domain equation is discretized using a finite-difference approach with uniform spatial meshes. The resulting tridiagonal system of equations is solved using the tridiagonal matrix algorithm (TDMA) to obtain the complex temperature profile along the sample. Boundary conditions as $T(x=-L/2)=T(x=L/2)=T_{\text{amb}}$ are applied at both ends of the sample as shown in Fig. 2d. While the physical heat transfer models used for measuring cross-plane and in-plane thermal conductivities differ, the experimental setup remains the same, as will be discussed in the following section. Only the modulation frequency of the laser is varied to obtain data for measurements in both directions.

2.3 Experimental Setup for Anisotropic Thermal Conductivity Measurement

The setup of the PT technique, a noncontact technique for measuring the thermophysical properties of samples in this work, is shown in Fig. 3a. A 785 nm laser (Cobolt 06-MLD) is modulated into square waves using a function generator (SRS

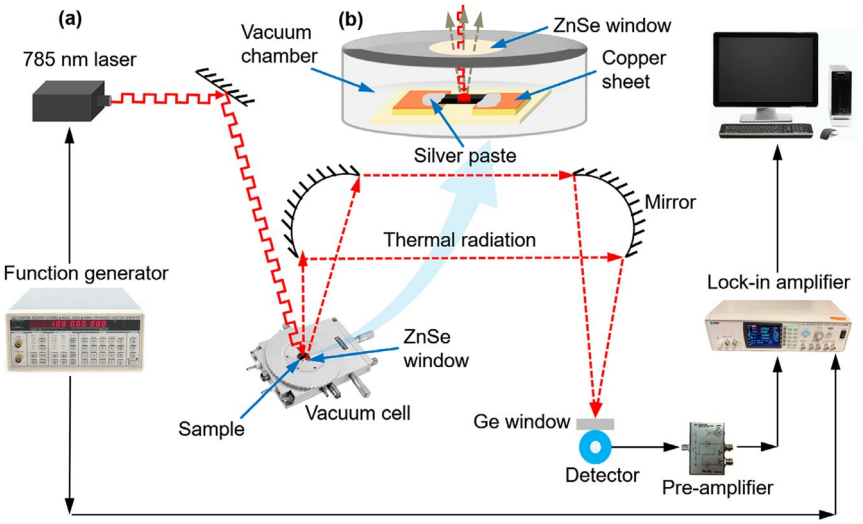

Fig. 3 (a) Schematic of PT experimental setup, (b) schematic of a suspended sample housed in the vacuum cell for PT measurements

DS345) and focused on the center of the sample, which is placed inside a vacuum cell (Linkam HFS350EV-PB4) mounted on a 3D nanostage (not shown in the figure). The modulated laser heating causes periodic temperature changes of the sample surface, which generate periodically varying thermal radiation. This emitted radiation carries information about the sample's thermophysical properties. The vacuum cell minimizes the air convection and improves the measurement accuracy. Such conditions are especially critical when measuring the in-plane thermal conductivity. The ZnSe window on the vacuum cell has a transmission range of 0.5 μm to 15 μm in wavelength [43]. This allows both the 785 nm laser and the sample's thermal radiation to pass through. According to Wien's displacement law [44], the peak wavelength of the thermal radiation from the sample is around 10 μm. The thermal radiation is directed by mirrors at a photoconductive infrared detector (Judson J15D12-M204-S01M-60), and the signal is then processed by a pre-amplifier (Teledyne Judson Technologies PA-102) and collected by a lock-in amplifier (NF LI5655). The lock-in amplifier measures the phase shift between the radiation signal and the laser input. To prevent any reflected laser light from reaching the detector, an anti-reflective coated germanium (Ge) window is placed in front of it. This Ge window blocks more than 99.9997 % of the laser light at the wavelengths used in this study.

Figure 3b shows the setup of a suspended narrow sample positioned between two copper electrodes, which act as heat sinks. The sample is secured with silver paste to ensure good thermal contact. Note that the same sample is used for both cross-plane and in-plane thermal conductivity measurements, which significantly simplifies the experimental process by reducing time, cost, and complexity. Also, the measured values reflect the intrinsic anisotropy of thermal conductivity. By varying only the modulation frequency, the measured heat transfer direction can be switched without

changing the sample position. To achieve high optical absorption at the laser wavelength, samples are often coated with a thin metallic layer such as iridium (Ir) or chromium (Cr). However, since the samples used in this work are naturally good absorbers, no additional coating is necessary. Before starting the experiment, we slightly adjust the sample position using the 3D nanostage (not shown in the figure) to maximize the signal's amplitude. This ensures that the detected thermal radiation originates from the same location where the laser is focused on, improving the accuracy of the measurement. Moreover, note that during data acquisition, the vacuum pump is turned off to avoid small vibrations that could slightly shift the sample's position and negatively affect the results. We ensure that the chamber maintains a good vacuum for several hours.

3 Results and Discussion

3.1 Calibration

Before starting measurements, the PT system must be calibrated to identify the phase shift introduced by equipment such as the detector, pre-amplifier, lock-in amplifier, and laser. If these shifts are left uncorrected, they can alter the true thermal radiation signal. To determine this calibration phase shift (ϕ_{cal}), the Ge window is removed, allowing the detector to directly receive the reflected laser light without spectral filtering. By subtracting ϕ_{cal} from the measured thermal radiation signal, we isolate the phase shift originating solely from thermal radiation, eliminating the influence of system-related delays. Figure 4a shows the calibration data for the equipment used in this study from 0.5 Hz to 1 MHz. In the calibration setup, the laser beam is directed straight onto the detector. Ideally, if there are no delays in the system, the phase shift would remain at 0° across all modulation frequencies. However, due to frequency-dependent response times in the components, deviations from this ideal behavior occur. The actual phase shift of the thermal radiation in the experiment is calculated by subtracting the calibration phase shift from the raw measured phase shift ϕ_{exp} as $\phi_{\text{real}} = \phi_{\text{exp}} - \phi_{\text{cal}}$.

3.2 Cross-Plane Thermal Conductivity Measurement

3.2.1 Measurement and Data Fitting

In this section, the cross-plane thermal conductivity of GP, GOP, and PRGP samples is measured using the PT technique. To extract directional thermal conductivities, frequency-dependent PT measurements are conducted. A higher frequency (f) range is selected to enhance sensitivity to the cross-plane direction heat conduction, and to make sure the in-plane heat transfer has negligible effect on the measurement. At higher modulation frequencies, the cross-plane thermal diffusion length ($\delta_{\perp}$) becomes smaller than, or comparable to the sample thickness, ensuring that heat flows mainly in the thickness direction. The thermal diffusion length can be obtained

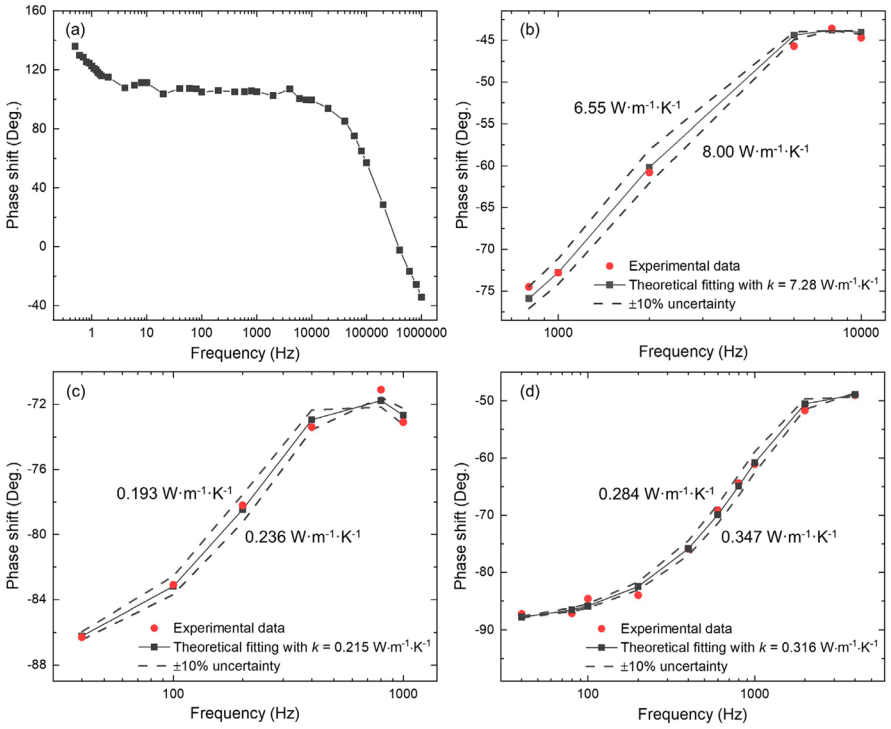

Fig. 4 (a) Calibration phase shift as a function of modulation frequency for direct laser irradiation onto the PC detector for 785 nm wavelength laser. Data fitting of phase shift for the thermal radiation from the sample surfaces for (b) GP, (c) GOP, and (d) PRGP, corresponding to cross-plane thermal conductivity measurements using the PT technique. Dashed lines indicate ± 10 % uncertainty in the thermal conductivity used for the theoretical fitting

using the relation $\delta_{\perp} = \sqrt{\alpha_{\perp}/(\pi f)}$, where $\alpha_{\perp} = k_{\perp}/(\rho c_p)$. This relation is used to estimate the appropriate modulation frequencies for cross-plane thermal conductivity measurements. Based on the sample thicknesses and estimated cross-plane diffusivities, the characteristic frequencies are calculated as 1727, 132, and 429 Hz for GP, GOP, and PRGP, respectively. The initially estimated frequency range is subsequently fine-tuned to maximize the signal-to-noise ratio during measurement. For reliable 1D cross-plane measurements, the modulation frequency must be chosen such that the thermal diffusion length is comparable to or slightly smaller than the sample thickness (i.e., $\delta <$ thickness). If $\delta >>$ sample thickness, heat penetrates entirely through the sample and becomes sensitive to the environment, reducing the sensitivity to the sample's cross-plane conductivity. On the other hand, if $\delta <<$ sample thickness, heat is confined too close to the surface, also reducing the sensitivity to cross-plane thermal transport. Furthermore, the in-plane thermal diffusion length $\delta_{\parallel} = \sqrt{\alpha_{\parallel}/(\pi f)}$ should be smaller than the laser beam radius (0.6 mm: see Sect. 3.3) during our cross-plane thermal conductivity measurements. This condition minimizes the in-plane heat transfer within the irradiated region, making the cross-plane

1D heat conduction model physically sound. All these criteria are satisfied in our experiments, confirming that thermal transport is effectively 1D along the cross-plane direction at the selected modulation frequencies shown in Fig. 4b–d.

Figure 4b–d shows the experimental phase shift data (ϕ_{real}) and the theoretical fitting for GP, GOP, and PRGP, respectively. The cross-plane thermal conductivity of GP, GOP, and PRGP samples is obtained to be 7.28 $W{\cdot}m^{-1}{\cdot}K^{-1}$, 0.215 $W{\cdot}m^{-1}{\cdot}K^{-1}$, and 0.316 $W{\cdot}m^{-1}{\cdot}K^{-1}$, respectively, as reported in Table 1. Note that the interfacial thermal resistance (ITR) between the sample and surrounding environment, which is vacuum in this work, has been considered a very small value of 10^{-9} $m^2{\cdot}K{\cdot}W^{-1}$. This has negligible effect considering the much larger thermal resistance of the surrounding. The experimental details are summarized in Table 1. Density values are obtained from Ref. [40], while the specific heat capacity of GOP and PRGP is extrapolated for room temperature (25 °C) from our previous work [45]. The specific heat capacity of GP is assumed to be the same as that of graphite (709 $J{\cdot}kg^{-1}{\cdot}K^{-1}$). Although GP and graphite differ structurally, their specific heat capacities are expected to be very similar [46].

Regarding the validity of the photothermal technique for measuring the cross-plane thermal conductivity of μm-thick suspended samples, we have conducted rigorous and systematic experiments and analysis for reference samples including SiO_2 wafer (92 μm thick) and crystalline sapphire (55 μm thick). The measurement results agree with the reference data with less than 10 % deviation. More details can be found in our recent work [47]. Also the repeatability of the measurements has been studied rigorously, and the measured phase shift usually has a standard deviation of less than 0.2°. However, even from the same batch, when different samples are cut for measurements, the measured phase shift will have changes from sample to sample. This is reasonable considering the non-uniformity of the sample, and has no effect on the measurement of a specific sample.

3.2.2 Physics Behind the Measurement Data

The cross-plane thermal conductivity of GP obtained in this study is consistent with the reported range of 5.7 $W{\cdot}m^{-1}{\cdot}K^{-1}$ to 6.8 $W{\cdot}m^{-1}{\cdot}K^{-1}$ for graphite [44]. The significantly lower cross-plane thermal conductivity of GP compared with its in-plane counterpart (discussed later) is attributed to the weak van der Waals

Table 1 Experimental details and fitted results of cross- and in-plane thermal conductivity measurements using PT technique

Sample	Thickness [μm]	Density [$kg{\cdot}m^{-3}$]	Specific heat [$J{\cdot}kg^{-1}{\cdot}K^{-1}$]	Thermal conductivity [$W{\cdot}m^{-1}{\cdot}K^{-1}$]		Thermal anisotropy ratio (Θ)
				Cross-plane	In-plane	
GP	31	1623	709	7.28	690	94.8
GOP	20	1357	780	0.215	0.78	3.63
PRGP	10	1466	760	0.316	2.9	9.18

interactions between adjacent graphene layers, which permit only low-frequency phonon modes to contribute to heat conduction [48, 49]. Notably, Han et al. [50] reported the cross-plane thermal conductivity of GP as 6.08 ± 0.6 $W \cdot m^{-1} \cdot K^{-1}$ for the same GP, but using the pulsed laser-assisted thermal relaxation 2 (PLTR2) technique. Their result closely aligns with our data. Furthermore, Li et al. [51] reported the cross-plane thermal conductivity of 4.83 $W \cdot m^{-1} \cdot K^{-1}$ for a graphene film. The difference among these measurements is largely due to the structure variation from sample to sample. It is noted that even for the same batch of sample, the structure is not uniform, which will cause thermal conductivity variation. For the GP measured in this work, we have cut another piece from the raw sample, and measured the thermal conductivity at different locations. It is observed the thermal conductivity varies from 5.19 $W \cdot m^{-1} \cdot K^{-1}$ to 5.80 $W \cdot m^{-1} \cdot K^{-1}$, confirming the structure variation in space.

Using the PLTR2 method, Han et al. [45] reported the cross-plane thermal conductivity of 0.16 $W \cdot m^{-1} \cdot K^{-1}$ for GOP and 0.14 $W \cdot m^{-1} \cdot K^{-1}$ for PRGP at 295 K. Hong et al. [52] obtained a value of 0.12 $W \cdot m^{-1} \cdot K^{-1}$ for an reduced graphene oxide (RGO) sample using the laser flash technique, attributing the low value to voids incorporated between layers. The cross-plane thermal conductivity of GO has also been reported as 0.114 $W \cdot m^{-1} \cdot K^{-1}$ [53]. Renteria et al. [54] reported the cross-plane thermal conductivity of GO to be 0.18 $W \cdot m^{-1} \cdot K^{-1}$, and a significantly lower value of 0.09 $W \cdot m^{-1} \cdot K^{-1}$ for RGO films annealed at 1000 °C, measured at 20 °C. They attributed the very low thermal conductivity of the RGO sample to the presence of air pockets between the layers during the annealing process and the partial restoration of sp^2 bonds within the atomic planes. Our measured cross-plane thermal conductivity for GOP (0.215 $W \cdot m^{-1} \cdot K^{-1}$) is consistent with the values reported in literatures, while the value for PRGP (0.316 $W \cdot m^{-1} \cdot K^{-1}$) is comparatively higher. The PRGP sample used in this study is commercially obtained and tested as received, with the exact reduction conditions unknown. It is likely that the PRGP samples reported in the literature are subjected to different reduction processes or levels of reduction and restoration of the sp^2 carbon network, potentially introducing more defects and structural disorder, which could explain their lower thermal conductivity values. Furthermore, variations in the extent of chemical reduction can also influence the specific heat capacity [45].

In data processing for GP and PRGP, our fitting is conducted by fitting both the optical absorption depth and cross-plane thermal conductivity. It is found that the optical absorption depths for these two samples are extremely small and confined to a shallow subsurface region, consistent with their relatively intact sp^2 carbon networks and low oxygen content. Varying the optical absorption depth over a reasonable range (10–100 nm) resulted in negligible changes in the fitted thermal conductivity, indicating minimal sensitivity of the phase response to this parameter. In contrast, for GOP, the optical absorption depth is found to be relative long (9.47 μm) and has a pronounced influence on the phase response due to its higher disorder and oxygen-containing functional groups.

3.2.3 Uncertainty Analysis and Discussion

To quantify the accuracy of the fitting between the experimental data and theoretical model, the root mean square error (RMSE) is calculated using the least square method. The RMSE is defined as the square root of the average of the squared differences between the experimental $\left(y_i\right)$ and the corresponding fitted values $\left(\hat{y}_i\right)$ as $\sqrt{\sum_{i=1}^{n}\left(y_i-\hat{y}_i\right)^2 \Big/ n}$, providing a reliable measure of the overall deviation between the model and the data. The RMSE between the experimental and fitted phase shift values is $\pm 0.86°$ for GP, $\pm 0.39°$ for GOP, and $\pm 0.84°$ for PRGP, which we report as uncertainty in the fitted phase shift. The dashed lines in Fig. 4b–d show phase shift simulations when the thermal conductivity is varied by ± 10 % from the best-fit value. Even this small variation in thermal conductivity leads to a noticeable change in phase shift, up to 2.1° for GP, 0.9° for GOP, and 2.0° for PRGP. This highlights the high sensitivity of fitting for thermal conductivity determination. It should be noted that these values indicate the phase shift difference between the best-fit case and the cases with a 10 % change in thermal conductivity. This strong dependence indicates that even minor mismatches between experimental and theoretical phase shifts correspond to meaningful changes in thermal conductivity, enabling reasonably precise thermal conductivity determination. In the studied frequency range, the phase sensitivity is approximately $< 0.5°$ per 5 % change in thermal conductivity. Our uncertainty analysis focuses on phase shift measurement, examining how the level of RMSE in the phase shift influences the resulting thermal conductivity. The same uncertainty analysis is used for the in-plane thermal conductivity measurement. The uncertainty of thermal conductivity caused by the thickness, density, and specific heat data of the samples is far less than that of phase shift measurement. Therefore their effects are not included here.

The above sensitivity analysis highlights the importance of selecting an appropriate frequency range for the experiment. For instance, in the case of GP sample (Fig. 4b), at frequencies above 4000 Hz, the phase shift curves for different thermal conductivities converge, making it difficult to distinguish between them. At such high modulation frequencies, the thermal penetration depth becomes much smaller than the film thickness, confining the temperature oscillations to a shallow sub-surface region. As a result, the phase shift becomes largely insensitive to the bulk cross-plane thermal conductivity, leading to a plateau of the phase shift versus frequency response and a reduction in fitting accuracy. Therefore, the use of lower frequency data, where thermal waves penetrate deeper into the sample but remain within the sample thickness, is critical for accurately extracting the cross-plane thermal conductivity. Moreover, at very low frequencies, the chance of contributions from both in-plane and cross-plane heat conduction increases, which can introduce additional uncertainty into the measurement and data interpretation.

Note that for the cross-plane thermal conductivity measurements, a limited number of modulation frequencies (typically 5–10 points) are used. This number is sufficient for reliable thermal conductivity extraction for several reasons. First, the selected frequencies span a wide range and cover the region in which the phase shift

exhibits strong sensitivity to the cross-plane thermal conductivity; and the phase shift separation between the lowest and highest selected frequencies is significant. Also the large phase separation between adjacent frequencies ensures that each data point provides substantial independent information for parameter fitting. Second, the photothermal data in this work are acquired manually rather than through automated frequency sweeping, with an emphasis on signal stability and measurement accuracy at each selected frequency. While a larger number of frequency points could in principle be collected by extending the duration of the experiment, the present data density is sufficient to uniquely determine the cross-plane thermal conductivity of the studied samples without compromising accuracy.

The laser-induced temperature rise is estimated using a radial heat diffusion model suitable for a suspended thin film. With an absorbed power of around 12 mW in our measurement, a laser spot radius of 0.6 mm, and an in-plane thermal conductivity of ~ 0.8 $W{\cdot}m^{-1}{\cdot}K^{-1}$, the maximum temperature increase is estimated to be ~ 4 K for GOP, which is the highest among the three samples. This confirms that laser-induced heating during the measurements is negligible, and will not cause structural damage of the sample.

3.3 In-Plane Thermal Conductivity Measurement

3.3.1 Measurement Data and Physics

In this section, the in-plane thermal conductivity of GP, GOP, and PRGP samples is measured using the PT technique. As previously discussed, the heat flow direction can be controlled by adjusting the modulation frequency. To enhance sensitivity to in-plane heat conduction, a low frequency range (< 1.5 Hz) is selected. At these frequencies, the cross-plane thermal diffusion length much exceeds the sample thickness. As a result, the in-plane heat diffusion along the suspended samples determines the phase shift. The estimated modulation frequencies for in-plane thermal conductivity measurements of GP, GOP, and PRGP are 0.48, 0.22, and 0.92 Hz, respectively, based on the sample lengths and the estimated in-plane thermal diffusivities. Additionally, in the width direction, the samples have a width of ~ 1 mm, which is fully covered by the laser beam (1.2 mm diameter), ensuring negligible lateral thermal gradients across the width. This is important for ensuring the heat conducts along the length direction during in-plane thermal conductivity measurements. It is important to note that the lower frequency limit of the NF LI5655 lock-in amplifier is 0.5 Hz. Figure 5 shows the experimental phase shift data with theoretical fittings for GP, GOP, and PRGP. The extracted in-plane thermal conductivities are 690 $W{\cdot}m^{-1}{\cdot}K^{-1}$, 0.78 $W{\cdot}m^{-1}{\cdot}K^{-1}$, and 2.9 $W{\cdot}m^{-1}{\cdot}K^{-1}$ for GP, GOP, and PRGP, respectively (see Table 1). In previous two works published by our group on the same GP sample using different techniques, the in-plane thermal conductivity was reported in the ranges of 616–642 $W{\cdot}m^{-1}{\cdot}K^{-1}$ [24] and 634–710 $W{\cdot}m^{-1}{\cdot}K^{-1}$ [40], demonstrating good agreement with the result of this study. Additionally, for the same GOP and PRGP samples, another study from our group reported thermal reffusivities (i.e., the inverse of thermal diffusivity) of 13.85×10^5 and

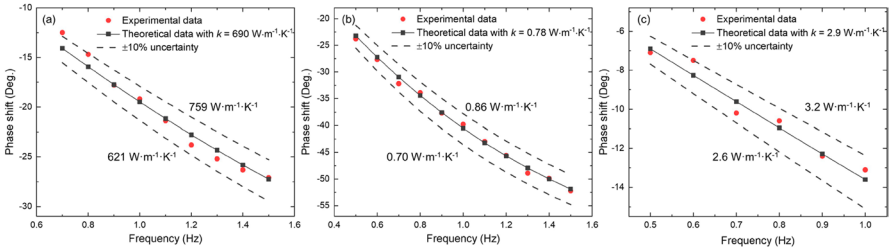

Fig. 5 Data fitting of phase shift for the thermal radiation from the sample surface for (b) GP, (c) GOP, and (d) PRGP, corresponding to in-plane thermal conductivity measurements using the PT technique. Dashed lines indicate ± 10 % uncertainty in the thermal conductivity used for the theoretical fitting

$(3.68–4.27)\times10^5$ s·m^{-2}, corresponding to thermal conductivities of 0.69 W·m^{-1}·K^{-1} and 2.43–2.83 W·m^{-1}·K^{-1} ($k = \alpha\rho c_p$), respectively, closely matching the results obtained in this work. Additionally, as expected, the thermal conductivity of PRGP in both in-plane and out-of-plane directions is higher than that of GOP, due to the partial removal of oxygen-containing functional groups, which reduces phonon scattering and facilitates more effective heat transfer through the partial restoration of the sp^2 carbon network.

3.3.2 Uncertainty Analysis and Discussion

The RMSE values for the in-plane thermal conductivity fitting are ± 0.83° for GP, ± 0.60° for GOP, and ± 0.48° for PRGP. Moreover, the dashed lines in each plot of Fig. 5 represent the ± 10 % uncertainty bound for the theoretical phase shift curves. These bounds provide a visual representation of the sensitivity of the model to changes in thermal conductivity and illustrate the confidence range around the best-fit curve.

In the simulation for data fitting, key parameters such as volumetric heat capacity, sample length, and laser spot size are required. The volumetric heat capacity values are the same as those used in the cross-plane measurements. Sample lengths of 2 cm for GP and 1 mm for both GOP and PRGP are selected. The shorter lengths of GOP and PRGP are critical for minimizing radiation heat loss, while a longer length for GP is suitable due to its high in-plane thermal conductivity. Generally, the radiative heat loss causes an overestimated thermal diffusivity as $4P\varepsilon\sigma T_0^3L^2/\left(\rho c_p A\pi^2\right)$ [55], where ε is the emissivity (approximated as 1 here), σ the Stefan-Boltzmann constant, T_0 the room temperature, L the sample length, P the sample's circumference, and A the sample's cross-sectional area. For thin-film samples of thickness z, this equation is simplified as $8\varepsilon\sigma T_0^3L^2/\left(\rho c_p z\pi^2\right)$, and the radiation-induced thermal diffusivity values are calculated to be 1.32×10^{-5} m^2·s^{-1} for GP, 6.14×10^{-8} m^2·s^{-1} for GOP, and 1.13×10^{-7} m^2·s^{-1} for PRGP. These values are significantly smaller than the corresponding measured thermal diffusivities of 5.99×10^{-4} m^2·s^{-1} for GP, 7.29×10^{-7} m^2·s^{-1} for GOP, and 2.69×10^{-6} m^2·s^{-1} for PRGP. Therefore, the contribution of radiation effect to the overall in-plane heat transfer is negligible in this study.

For the laser spot size measurement, as mentioned earlier, the radial intensity distribution of a Gaussian beam is described by $I = I_0 \exp\left(-\left(x - x_0\right)^2 \Big/ r_0^2\right)$. The knife-edge technique [56] is employed to characterize the laser beam profile and determine the laser power distribution. In this technique, a sharp edge is translated across the laser beam path along the x direction, while the transmitted power is recorded at each position with a step size of 10 μm. By integrating the Gaussian intensity distribution along the beam cross-section, the cumulative laser power as a function of edge position x is given by $P = P_0\left[1 + \mathrm{erf}\left(\left(x - x_0\right)\Big/ r_0\right)\right]$, where the P is the laser power at the position x, and P_0 is the total beam power. The knife-edge data are fitted to this equation, and the beam radius r_0 is determined to be 0.6 mm. Our sample width is chosen to be 1 mm, less than the laser spot diameter (1.2 mm). Therefore, in the heating region, the temperature difference in the width direction can be neglected.

The measured thermal conductivities reveal pronounced anisotropy that directly reflects the structural differences among the three graphene-based samples. The thermal anisotropy ratio (Θ), which is a ratio of the in-plane thermal conductivity over the cross-plane one, is summarized in Table 1. GP exhibits the highest in-plane thermal conductivity and the largest thermal anisotropy ratio (94.8), consistent with its low defect density and well-aligned layered structure, as confirmed by Raman spectra and optical imaging. In contrast, GOP shows a significant reduction in both in-plane thermal conductivity and thermal anisotropy ratio (3.63), indicating that oxidation introduces defects that enhance phonon scattering and weaken interlayer coupling. PRGP demonstrates partial recovery of thermal transport, highlighting that reduction can mitigate, but not completely eliminate the structural disorder. The thermal anisotropy ratio quantifies these effects: 94.8 for GP, 3.63 for GOP, and 9.18 for PRGP. These results illustrate a clear correlation between structural integrity, defect density, and directional thermal transport, emphasizing that even moderate chemical modification can dramatically influence the anisotropic thermal behavior in graphene-based materials.

From a phonon transport perspective, the XRD-derived interlayer spacing plays a critical role in determining the phonon mean free path. In highly crystalline GP, the interlayer spacing of ~ 3.35 Å and well-aligned structure enable long phonon mean free path due to reduced boundary and defect scattering. The phonon mean free path can be expressed as $l = v\tau$, where v is the phonon group velocity and τ is the relaxation time. In GP, both intrinsic scattering and interlayer coupling allow a relatively large τ, leading to a high thermal conductivity. However, the oxidation in GOP introduces functional groups that not only increase interlayer spacing but also act as strong phonon scattering centers, significantly reducing τ. In addition, the increased spacing weakens interlayer coupling, limiting cross-plane phonon transport and further shortening the effective phonon mean free path. For PRGP, although partial reduction restores some sp^2 bonding, residual defects and incomplete structural recovery continue to limit phonon lifetimes. Consequently, the progressive reduction in phonon mean free path from GP to PRGP to GOP directly explains the observed decrease in thermal conductivity and anisotropy. These results highlight that oxidation-induced structural expansion and disorder,

as evidenced by XRD, are key factors governing phonon scattering mechanisms in graphene-based structures.

3.3.3 Location Sensitivity in In-Plane Thermal Conductivity Measurement

As mentioned earlier, the laser irradiates the center of the suspended sample, and the sample position is slightly adjusted to maximize the signal. This ensures that laser heating and thermal radiation sensing occur at the same location. However, this location may not coincide precisely with the geometric center of the sample. Here we present how the location could affect the in-plane thermal conductivity measurement. Figure 6a–c shows a theoretical analysis of phase shift at low frequencies when the heating/sensing position is offset by up to 10 % from the midpoint of the sample length for GP, GOP, and PRGP, respectively. In the simulation, the thermal radiation sensing length is taken as 1 mm, corresponding to the length of the detector, and the average phase shift over this length is calculated. For GP (2 cm length), Fig. 6a shows that a 10 % position offset results in only a 4.2 % difference in phase shift across all frequencies, which has negligible effect on the fitting result. For GOP (Fig. 6b) and PRGP (Fig. 6c) (1 mm length), the phase shift differences are even smaller, 0.7 % for GOP and 0.6 % for PRGP, because the sample and sensing lengths are the same. Therefore, a 10 % deviation from the sample midpoint in laser heating and thermal radiation sensing has a negligible impact on the results.

4 Benchmarking of In-Plane Thermal Conductivity

To the best of our knowledge, this is the first time the PT technique is used to measure the in-plane thermal conductivity of suspended samples. The measurement accuracy is also evaluated by benchmarking against the well-established TET technique. The TET technique, originally developed by our group in 2007 [23], enables precise determination of the thermal diffusivity of suspended fiber-like and thin-film materials. Over the years, it has been applied to a broad range of samples, including carbon nanocoils, carbon nanotubes, polypropylene separators, and various other materials [40, 55, 57–60]. Figure 7a shows the physical

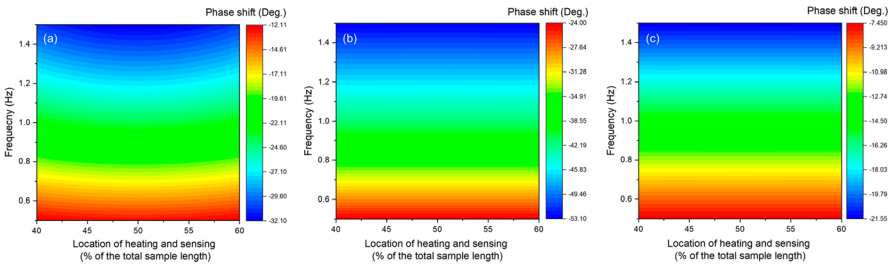

Fig. 6 Phase shift sensitivity based on location of laser heating and thermal radiation sensing for in-plane thermal conductivity for (a) GP, (b) GOP, and (c) PRGP

principle of this technique. In the measurement, the sample is mounted across a trench and affixed to two aluminum electrodes with silver paste to ensure robust electrical and thermal contact. During measurement, a step DC current, supplied by a current source (Keithley 6221), is applied. The resulting Joule heating raises the sample's temperature and consequently changes its electrical resistance. This resistance change is monitored as a transient variation in the measured voltage over the sample using an oscilloscope (Tektronix DPO3052). The heating interval is selected so that the sample reaches the steady state, with adequate cooling time between current pulses to avoid cumulative heating. The resulting voltage–time (*V-t*) profile, which characterizes the sample's transient thermal behavior, is analyzed to extract its effective thermal diffusivity (α_{eff}). For non-conductive materials coated with a thin conductive layer, or when radiative heat loss is significant, these effects can be accounted for and removed during post-analysis.

Because of the high aspect ratio (length-to-thickness) of the samples, heat transfer can be considered 1D along the length. All experiments are performed under high vacuum (< 0.2 mtorr) to minimize convective effects. The transient heat conduction along the sample (*x*-direction) follows the 1D heat conduction equation as Ref. [23].

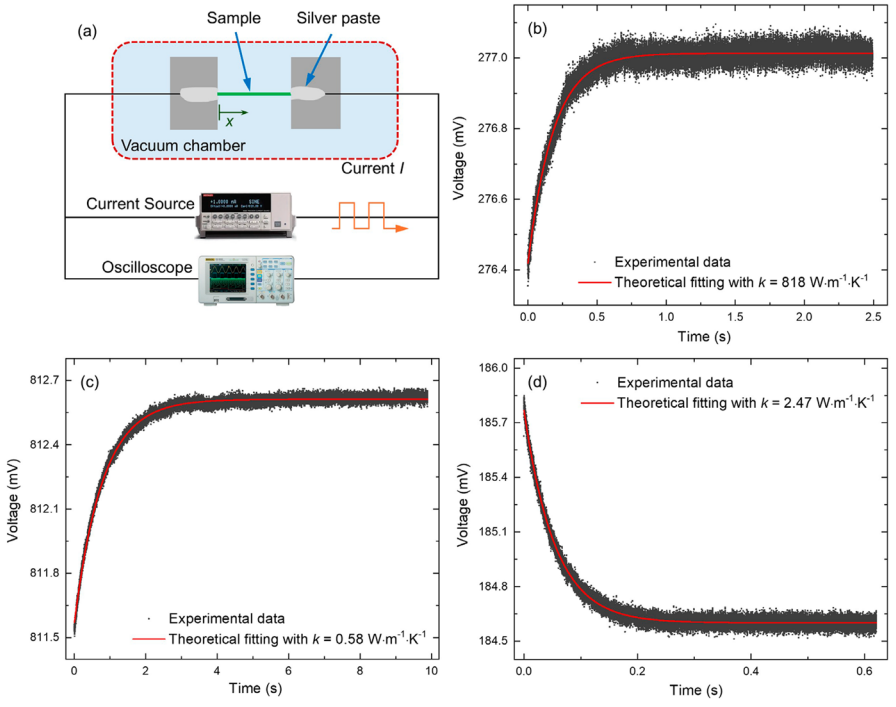

Fig. 7 (a) Experimental setup of the TET technique. Data fitting of voltage signals obtained from oscilloscope for (b) GP, (c) GOP, and (d) PRGP

$$\frac{\partial(T\rho c_p)}{\partial t} = \frac{\partial}{\partial x}\left(k_{\parallel}\frac{\partial T}{\partial x}\right) + \dot{q}_0. \tag{16}$$

here, $\dot{q}_0$ [W·m^{-3}] represents the volumetric heat generation due to the applied current. Using Green's function solution, the normalized temperature rise along the length can be expressed as

$$T^* = \frac{96}{\pi^4}\sum_{m=1}^{\infty}\frac{1-\exp[-(2m-1)^2\pi^2\alpha_{\text{eff}}t/L^2]}{(2m-1)^4}, \tag{17}$$

where L is the sample length and t is time. A simplified version of Eq. 17 as an exponential model for $T^*(t)$ has been developed as

$$T^* = 1-\exp(-\pi^2\alpha_{\text{eff}}t/L^2). \tag{18}$$

Since the transient voltage change is directly proportional to the temperature rise, the experimental *V*-*t* data can be fitted using the following expression to determine α_{eff}[61]

$$V = b_1 + b_2\exp(-\pi^2\alpha_{\text{eff}}t/L^2), \tag{19}$$

where b_1, b_2, and α_{eff} are fitting parameters extracted from the regression.

The samples of GP, GOP, and PRGP are prepared for testing using the TET technique. The dimensions and obtained thermal diffusivities and conductivities of these three samples are summarized in Table 2. For consistency, the same density and specific heat capacity values used in the PT technique analysis are applied here. The sample thicknesses are also identical to those used in the PT measurements. By fitting the TET signals using Eq. 19, as shown in Fig. 7b–d, the obtained effective thermal diffusivity for GP, GOP, and PRGP samples is 7.57×10^{-4} m^2·s^{-1}, 7.08×10^{-7} m^2·s^{-1}, and 3.01×10^{-6} m^2·s^{-1}, respectively. Since GOP is non-conductive, it is coated with a very thin layer (~10 nm thick) of Ir film to enable TET measurement. To account for both radiation and coating effects, it has been shown that for a film-like sample, the real thermal diffusivity (α_{real}) can be calculated as $\alpha_{\text{real}} = \alpha_{\text{eff}} - \left[8\varepsilon\sigma T_0^3L^2/\left(\rho c_p z\pi^2\right)\right] - \left[L_{\text{Lorenz}}T_0L/RA\rho c_p\right]$. Here, L_{Lorenz} is the Lorenz number, which is ~3.69×10^{-8} W·Ω·K^{-2} for a 10 nm thick Ir coating [62], and R is the electrical resistance of the sample during the TET experiment. Therefore, the real thermal diffusivity is calculated to be 7.11×10^{-4} m^2·s^{-1} for GP, 6.07×10^{-7}

Table 2 Experimental details and fitted results of in-plane thermal conductivity using the TET technique

Sample	Length [mm]	Width [mm]	Real thermal diffusivity [m^2·s^{-1}]	Thermal conductivity [W·m^{-1}·K^{-1}]
GP	37.191	0.270	7.11×10^{-4}	818
GOP	1.271	0.665	6.07×10^{-7}	0.64
PRGP	2.350	0.645	2.38×10^{-6}	2.65

$m^2 \cdot s^{-1}$ for GOP, and 2.38×10^{-6} $m^2 \cdot s^{-1}$ for PRGP, corresponding to thermal conductivities of 818 $W \cdot m^{-1} \cdot K^{-1}$, 0.64 $W \cdot m^{-1} \cdot K^{-1}$, and 2.65 $W \cdot m^{-1} \cdot K^{-1}$, respectively. These values agree well with the PT technique results, confirming their validity. The slight discrepancy between the PT and TET results does not arise from experimental inaccuracy but rather from sample-to-sample variations. In our lab, Xie et al. [40] previously measured the thermal diffusivity of multiple samples prepared from the same material (e.g., PRGP) and observed noticeable differences. This indicates that even nominally identical samples can exhibit variability, particularly when the material is not a perfect single crystal. Different sections of the same material may possess microstructural variations that lead to differences in thermal transport properties. In fact, Xie et al. [40] reported variations of up to ~ 50 % in thermal diffusivity among samples cut from different sections of the same PRGP material.

It needs to be noted that the frequency resolving method developed in this work can also be applied to supported micro/nanoscale materials and bulk materials to measure their anisotropic thermal conductivity. For the cross-plane (direction along the laser beam irradiation) thermal conductivity measurement, a carefully chosen high frequency range can be used to exclude the effect of lateral heat conduction. However, for the in-plane thermal conductivity measurement, even at low frequencies, the cross-plane heat conduction in the substrate/bulk part could still be important, and will strongly affect the measured signal. This will somehow reduce the measurement sensitivity. A suspended sample could eliminate this effect and dramatically improve the sensitivity of in-plane thermal conductivity measurement.

5 Conclusion

This study rigorously measured the anisotropic thermal conductivity of graphene-based films and investigated their real thermal anisotropy ratio. The thermal anisotropy ratio in graphene-based papers is governed primarily by material structure. GP, GOP, and PRGP exhibited distinct oxidation and reduction states that lead to measurable differences in microstructure, as evidenced by Raman spectroscopy and optical microscopy. These structural variations directly control both the magnitude and anisotropy of thermal conductivity by modifying phonon scattering, interlayer coupling, and flake alignment. Using a frequency-resolved photothermal (PT) technique, both in-plane and cross-plane thermal conductivities were extracted from the same suspended specimen at a fixed measurement location. This single-sample approach eliminates preparation-induced structural variation that can arise when separate samples or techniques are used, enabling a faithful determination of intrinsic thermal anisotropy ratio. The measured cross-plane and in-plane thermal conductivities are 7.28 $W \cdot m^{-1} \cdot K^{-1}$ and 690 $W \cdot m^{-1} \cdot K^{-1}$ for GP, 0.215 $W \cdot m^{-1} \cdot K^{-1}$ and 0.78 $W \cdot m^{-1} \cdot K^{-1}$ for GOP, and 0.316 $W \cdot m^{-1} \cdot K^{-1}$ and 2.9 $W \cdot m^{-1} \cdot K^{-1}$ for PRGP, respectively, showing good agreement with literature values and independent transient electro-thermal measurements. The slightly higher cross-plane thermal conductivity observed for PRGP compared with reported values is attributed to differences in reduction conditions, layer stacking, and microstructural organization. Importantly, the resulting thermal anisotropy ratios are 94.8 for GP, 3.63 for GOP,

and 9.18 for PRGP. These values provide a robust and physically meaningful basis for comparing graphene-based papers and reveal a clear correlation between oxidation-induced disorder and reduced thermal anisotropy. Overall, this work highlights the critical role of material structure in governing directional thermal transport and demonstrates that the frequency-resolved PT approach offers a versatile and non-destructive platform for investigating anisotropic thermal conductivity in a broad range of thin-film materials relevant to electronics, energy storage, and thermal management applications.

Acknowledgements We utilized AI-powered tools to check grammar and enhance the academic quality of the text, which was primarily written by the authors.

Author Contribution Investigation: Mahya Rahbar (equal), Amin Karamati (equal), Jiwen Li (equal); Data curation: Mahya Rahbar (equal), Amin Karamati (equal); Formal analysis: Mahya Rahbar (equal), Amin Karamati (equal), Lijun Zhang (equal); Writing–original draft: Mahya Rahbar (equal), Amin Karamati (equal); Conceptualization: Lijun Zhang, Xinwei Wang; Funding acquisition: Xinwei Wang; Writing–review and editing: Lijun Zhang, Xinwei Wang.

Data Availability Data are available upon request from readers.

Declarations

Conflict of interest The authors declare no competing interests.

References

1. Y. Zhang, D. Zhao, R. Xu, Y. Liu, M. Liu, J. Wang, Int. J. Thermophys. **47**(4), 58 (2026). https://doi.org/10.1007/s10765-026-03736-4
2. S.E. Kim, F. Mujid, A. Rai, F. Eriksson, J. Suh, P. Poddar, A. Ray, C. Park, E. Fransson, Y. Zhong, Nature **597**(7878), 660 (2021)
3. F. Cheng, A. Alasli, R. Fujita, A. Ueno, T. Ishizaki, N. Sakatani, R. Endo, S. Arakawa, T. Nishi, T. Kobayashi, A. Tsuchiyama, H. Nagano, S. Tanaka, Int. J. Thermophys. **46**(10), 145 (2025). https://doi.org/10.1007/s10765-025-03563-z
4. L. Li, Y. Yu, G.J. Ye, Q. Ge, X. Ou, H. Wu, D. Feng, X.H. Chen, Y. Zhang, Nat. Nanotechnol. **9**(5), 372 (2014)
5. J. Yang, P. Hu, G. Yu, APL Mater. (2019). https://doi.org/10.1063/1.5054823
6. J.-H. Chu, J.G. Analytis, K. De Greve, P.L. McMahon, Z. Islam, Y. Yamamoto, I.R. Fisher, Science **329**(5993), 824 (2010)
7. M.K. Subramani, S. Mohan, T. Subramani, A. Sathishkumar, S.C. Kim, Int. J. Thermophys. **47**(3), 50 (2026). https://doi.org/10.1007/s10765-026-03719-5
8. N. Chowdhury, J. Sun, D.G. Cahill, ACS Appl. Polym. Mater. (2025). https://doi.org/10.1021/acsapm.4c03181
9. P. Jiang, X. Qian, R. Yang, J. Appl. Phys. (2018). https://doi.org/10.1063/1.5046944
10. J. Sun, G. Lv, D.G. Cahill, Rev. Sci. Instrum. (2023). https://doi.org/10.1063/5.0126717
11. T. Tian, K.D. Cole, Int. J. Heat Mass Transfer **55**(23–24), 6530 (2012)
12. L. Lu, W. Yi, D. Zhang, Rev. Sci. Instrum. **72**(7), 2996 (2001)
13. H. Jang, J.D. Wood, C.R. Ryder, M.C. Hersam, D.G. Cahill, Adv. Mater. **27**(48), 8017 (2015)
14. P. Jiang, X. Qian, R. Yang, Rev. Sci. Instrum. (2017). https://doi.org/10.1063/1.4991715
15. L. Tang, C. Dames, Int. J. Heat Mass Transfer **164**, 120600 (2021)
16. S. Huang, M. Segovia, X. Yang, Y.R. Koh, Y. Wang, P.D. Ye, W. Wu, A. Shakouri, X. Ruan, X. Xu, 2D Mater. **7**(1), 015008 (2019)
17. A.J. Schmidt, R. Cheaito, M. Chiesa, Rev. Sci. Instrum. (2009). https://doi.org/10.1063/1.3212673
18. D. Wang, H. Ban, P. Jiang, Appl. Phys. Rev. (2024). https://doi.org/10.1063/5.0191073

19. F. Takahashi, K. Ito, J. Morikawa, T. Hashimoto, I. Hatta, Jpn. J. Appl. Phys. **43**(10R), 7200 (2004)
20. M. Tanimoto, T. Yamagata, K. Miyata, S. Ando, ACS Appl. Mater. Interfaces **5**(10), 4374 (2013)
21. Q. Alahmad, M. Rahbar, A. Karamati, J. Bai, X. Wang, J. Power. Sources **580**, 233377 (2023). https://doi.org/10.1016/j.jpowsour.2023.233377
22. Q. Alahmad, M. Rahbar, M. Han, H. Lin, S. Xu, X. Wang, Int. J. Thermophys. **44**(11), 167 (2023)
23. J. Guo, X. Wang, T. Wang, J. Appl. Phys. (2007). https://doi.org/10.1063/1.2714679
24. M. Rahbar, M. Han, S. Xu, H. Zobeiri, X. Wang, Int. J. Heat Mass Transfer **202**, 123712 (2023). https://doi.org/10.1016/j.ijheatmasstransfer.2022.123712
25. S. Xu, X. Wang, AIP Adv. (2014). https://doi.org/10.1063/1.4898330
26. X. Wang, Z. Zhong, J. Xu, J. Appl. Phys. (2005). https://doi.org/10.1063/1.1854725
27. W.S. Hummers Jr., R.E. Offeman, J. Am. Chem. Soc. **80**(6), 1339 (1958)
28. V. Scardaci, G. Compagnini, C **7**(2), 48 (2021)
29. D. Graf, F. Molitor, K. Ensslin, C. Stampfer, A. Jungen, C. Hierold, L. Wirtz, Nano Lett. **7**(2), 238 (2007)
30. A.F. Sardinha, D.A. Almeida, N.G. Ferreira, J. Mater. Process. Technol. **9**(5), 10841 (2020)
31. J.-B. Wu, M.-L. Lin, X. Cong, H.-N. Liu, P.-H. Tan, Chem. Soc. Rev. **47**(5), 1822 (2018)
32. D. Lopez-Diaz, J.A. Delgado-Notario, V. Clericò, E. Diez, M.D. Merchan, M.M. Velázquez, Coatings **10**(6), 524 (2020)
33. S. Vollebregt, R. Ishihara, F. Tichelaar, Y. Hou, C. Beenakker, Carbon **50**(10), 3542 (2012)
34. S. Claramunt, A. Varea, D. Lopez-Diaz, M.M. Velázquez, A. Cornet, A. Cirera, J. Phys. Chem. C **119**(18), 10123 (2015)
35. E. Martins Ferreira, M.V. Moutinho, F. Stavale, M.M. Lucchese, R.B. Capaz, C.A. Achete, A. Jorio, Phys. Rev. B **82**(12), 125429 (2010)
36. D. López-Díaz, M. Lopez Holgado, J.L. García-Fierro, M.M. Velázquez, J. Phys. Chem. C **121**(37), 20489 (2017)
37. J. Maultzsch, S. Reich, C. Thomsen, Phys. Rev. B **70**(15), 155403 (2004)
38. G. Yasin, M. Arif, M. Shakeel, Y. Dun, Y. Zuo, W.Q. Khan, Y. Tang, A. Khan, M. Nadeem, Adv. Eng. Mater. **20**(7), 1701166 (2018)
39. V. Scardaci, G. Compagnini, Data Brief **38**, 107306 (2021)
40. Y. Xie, P. Yuan, T. Wang, N. Hashemi, X. Wang, Nanoscale **8**(40), 17581 (2016). https://doi.org/10.1039/c6nr06402g
41. Y. Hua, I. Al Keyyam, Y. Xie, X. Wang, J. Appl. Phys. (2025). https://doi.org/10.1063/5.0275419
42. I. Al Keyyam, M. Rahbar, N. Hunter, B. Li, T. Wang, E. Shi, X. Wang, Int. J. Heat Mass Transfer **226**, 125513 (2024)
43. G. Rusu, M. Diciu, C. Pirghie, E. Popa, Appl. Surf. Sci. **253**(24), 9500 (2007)
44. F.P. Incropera, D.P. DeWitt, T.L. Bergman, A.S. Lavine, *Fundamentals of heat and mass transfer* (Wiley, New York, 1996)
45. M. Han, Y. Xie, J. Liu, J. Zhang, X. Wang, Nanotechnology **29**(26), 265702 (2018)
46. E. Pop, V. Varshney, A.K. Roy, MRS Bull. **37**(12), 1273 (2012)
47. M. Rahbar, N. Van Velson, X. Wang, J. Laser Appl. (2026). https://doi.org/10.2351/7.0002004
48. J. Xiang, L.T. Drzal, Sol. Energy Mater. Sol. Cells **95**(7), 1811 (2011)
49. C.Y. Ho, R.W. Powell, P.E. Liley, J. Phys. Chem. Ref. Data **1**(2), 279 (1972)
50. M. Han, J. Liu, Y. Xie, X. Wang, Carbon **126**, 532 (2018). https://doi.org/10.1016/j.carbon.2017.10.070
51. X. Li, T. Zhang, R. Zhang, J. Liu, T. Tian, H. Han, K. Cao, Y. Su, Appl. Surf. Sci. (2025). https://doi.org/10.1016/j.apsusc.2025.163297
52. S. Hong, S.S. Yoo, P.J. Yoo, J. Mater. Chem. C **7**(30), 9380 (2019)
53. S. Jin, Q. Gao, X. Zeng, R. Zhang, K. Liu, X. Shao, M. Jin, Diamond Relat. Mater. **58**, 54 (2015)
54. J.D. Renteria, S. Ramirez, H. Malekpour, B. Alonso, A. Centeno, A. Zurutuza, A.I. Cocemasov, D.L. Nika, A.A. Balandin, Adv. Funct. Mater. **25**(29), 4664 (2015)
55. N. Hunter, A. Karamati, Y. Xie, H. Lin, X. Wang, ChemPhysChem **23**(23), e202200417 (2022). https://doi.org/10.1002/cphc.202200417
56. J.M. Khosrofian, B.A. Garetz, Appl. Opt. **22**(21), 3406 (1983)
57. J. Bai, A. Karamati, X. Duan, H. Lin, X. Wang, J. Phys. Chem. C **129**(11), 5754 (2025)
58. A. Karamati, C. Deng, W. Qu, X. Bai, S. Xu, G. Eres, X. Wang, J. Appl. Phys. (2023). https://doi.org/10.1063/5.0157932
59. S. Xu, H. Zobeiri, N. Hunter, H. Zhang, G. Eres, X. Wang, Nano Energy **86**, 106054 (2021). https://doi.org/10.1016/j.nanoen.2021.106054

60. R. Wang, H. Zobeiri, H. Lin, W. Qu, X. Bai, C. Deng, X. Wang, Carbon **147**, 58 (2019). https://doi.org/10.1016/j.carbon.2019.02.064
61. A. Karamati, M. Han, X. Duan, Y. Xie, X. Wang, Int. J. Heat Mass Transfer **233**, 126012 (2024)
62. Q. Alahmad, H. Lin, J. Liu, M. Rahbar, T.A. Kingston, X. Wang, Int. J. Thermophys. **46**(9), 141 (2025)

Authors and Affiliations

Mahya Rahbar[1] · Amin Karamati[1] · Jiwen Li[2] · Lijun Zhang[3] · Xinwei Wang[1]

✉ Lijun Zhang
ljzhang@shou.edu.cn

✉ Xinwei Wang
xwang3@iastate.edu

[1] Department of Mechanical Engineering, Iowa State University, Ames, IA 50011, USA

[2] Department of Electrical and Computer Engineering, University of Southern California, Los Angeles, CA 90089, USA

[3] College of Engineering Science and Technology, Shanghai Ocean University, 999 Huchenghuan Road, Shanghai 201306, People's Republic of China